Accessing power-law statistics under experimental constraints

Xavier Durang [1,*] Hyerim Ahn [2,3] Jae Youn Shim [2] Hye Yoon Park [2,3,†] and Jae-Hyung Jeon [1,‡]

[1]*Department of Physics, Pohang University of Science and Technology, Pohang 37673, Republic of Korea*

[2]*Department of Physics and Astronomy, Seoul National University, Seoul 08826, Republic of Korea*

[3]*Department of Electrical and Computer Engineering, University of Minnesota, Minneapolis, Minnesota 55455, USA*

(Received 7 June 2022; accepted 21 December 2022; published 12 January 2023)

Power-law distributions appear in a large variety of situations and influence our understanding of various physical phenomena. Their identification and characterization are notoriously difficult because of the large fluctuations inherent to empirical data and also because of the unknown range over which the power-law behavior holds. Furthermore, the data on which one is trying to detect power laws are affected by technical constraints and experimental limitations. Here, we show how a power-law distribution is modified by two fundamental limitations: the spatiotemporal resolution and the time window. We consider a time series of events or states and investigate the interevent time probability density function (PDF) or the PDF of the duration of a state. We present in detail how each limitation affects the PDF and derive mathematical expressions that relate the observed distribution to the true one: the resolution globally affects the shape of PDF while preserving the asymptotic exponent and the time window introduces a nonexponential cutoff. We demonstrate that, instead of looking for a simple power law in experimental data, one should fit the data with the modified PDF that we derived for given experimental constraints. We apply our theory to data from an experimental study of the transport of mRNA-protein complexes along dendrites. The presented mathematical theory widens our understanding of the identification and characterization of power-law distributions in experimental data and can be used in a broad spectrum of science fields.

DOI: 10.1103/PhysRevResearch.5.013011

I. INTRODUCTION

Found in critical phenomena [1–4], in systems with a critical self-organization [5], earthquake magnitudes [6], human mobility [7], animal foraging or distribution pattern of animal species [8], and transport in cells [9,10], power-law distributions in natural, technical, and living systems have attracted many research activities to understand their origins. The detection of such power-law distributions is a main subject of research that has lead to the well-known maximum likelihood method for the estimation of the power-law exponent, as developed in Ref. [11] and tested over many real-world data. More recently, this method has been used to solve the usual claim on whether or not real-world networks are scale-free, which means that their degree distribution should follow a power-law distribution [12,13].

In general, real-world data or typical experimental data consist of either time series of events or trajectories of specific objects. In the former case, the events are recorded over time [Fig. 1(a)], e.g., earthquake sequences [14], and the interevent time distribution is usually studied. In the latter, the location of an object is tracked over time, e.g., movement of labeled macromolecules within a cell [10,15–18]. Over the last decades, a large array of experimental techniques and analytical tools, such as the single-particle tracking technique, has been applied to characterize the microscopic behavior of biomolecules in living systems. The diffusion coefficient or the active transport properties are deduced from the measured trajectories, and microscopic models mimicking the observed behavior are constructed. For example, the motion of the β-actin mRNA-protein (mRNP) complex was shown to follow an aging Lévy walk [10]. However, estimation of the power-law exponent from such data is nontrivial because the experimental constraints often cause significant deviation from the original time distribution of the data.

When it comes to the study of transport phenomena, there were some efforts to develop a statistical method taking into consideration the experimental constraints and measurement errors in the determination of the diffusion coefficient and the anomalous diffusion exponent [19,20]. More recently, using machine-learning-based approaches, several groups extracted the anomalous exponent and inferred a stochastic model to describe experimental diffusion processes [21]. Bayesian inference methods have also been developed to extract the anomalous exponent from real data with errors and for detecting Lévy walks [22] and fractional or scaled Brownian motion [23]. For a short reminder, the anomalous diffusion of a single particle is conventionally classified by a power-law scaling of the mean-squared displacement:

$$\langle x^2(t)\rangle \propto t^{\alpha}, \tag{1}$$

*xdurang@postech.ac.kr
†hyp@umn.edu
‡jeonjh@postech.ac.kr

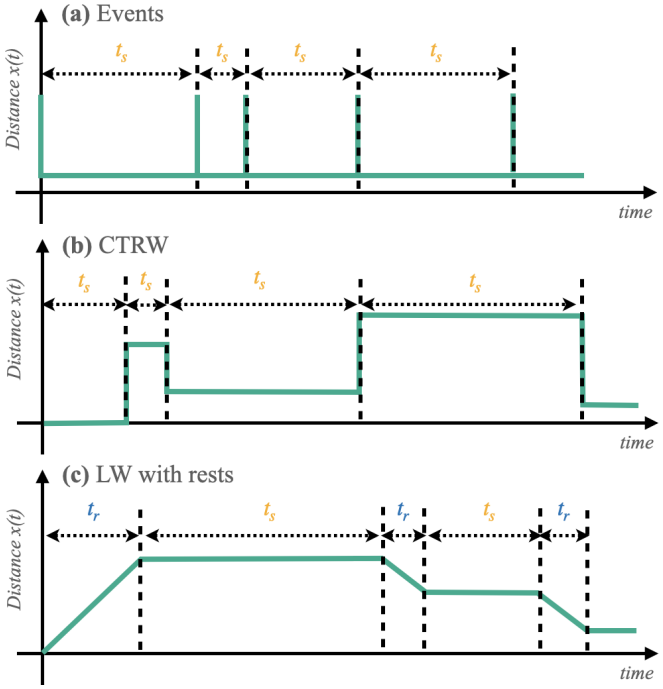

FIG. 1. Examples of stochastic processes under consideration. (a) Events occurring along the timeline, e.g., earthquakes. The quantity of interest is the PDF of the interevent time t_s. (b) Continuous-time random walk processes governed by $\psi_{\text{waiting}}(t_s)$, i.e., the PDF of waiting times t_s between successive jumps. The jumps are instantaneous and described by the PDF of jump length $\psi_{\text{jump}}(x)$. (c) A Lévy walk with rests [49]. It is a two-state process consisting of an alternation of a ballistically moving run phase and a "no-moving" rest phase. The occurrence times of both phases are independent, characterized by the corresponding PDFs, $\psi_{\text{run}}(t_r)$ and $\psi_{\text{rest}}(t_s)$, respectively.

where $\alpha \neq 1$ is referred to as the anomalous exponent. The diffusion process is called subdiffusion for $0 < \alpha < 1$ and superdiffusion for $\alpha > 1$ [24]. This power-law exponent appears in various areas such as target finding times [25] or cellular organization [26]. The generalized diffusion law (1) emerges due to the breakdown of the central limit theorem (CLT). One of the physical mechanisms violating the CLT is broad distributions in diffusion events, such as jump lengths or waiting times between successive jumps [24].

It is known that anomalous diffusion processes in this category are described by the diffusion models in the class of continuous-time random walk (CTRW) such as subdiffusive CTRW [Fig. 1(b)], Lévy walk (LW), and LW with rests [Fig. 1(c)]. They can be understood as a two-state process where the system stays in a state for a duration drawn from a given distribution; see the rest events in the subdiffusive CTRW [Fig. 1(b)] and run/rest events in the LW with rests [Fig. 1(c)]. For many single-particle tracking experiments, it has been reported that these models describe the microscopic transport dynamics successfully. Examples include the gamma burst pattern in a primate cerebral cortex [27], the motion of mRNA along the dendrites [10], the diffusion of microbeads in cytoskeletal filaments [28], the predator search behavior [29], the human mobility [30], the migration of swarming bacteria [31], the central pattern of locomotion of the Drosophila [32], and the T-cell motility in the brain [16].

In the aforementioned dynamic models such as time series of events or CTRW families, the knowledge on the distribution or its probability density function (PDF) of random event times is essential to classify the dynamics of the object. However, it is highly nontrivial to correctly obtain the corresponding time (or length) distribution in the experiments due to the limitations and errors of the measurement. For instance, in single-particle tracking experiments, the localization errors that originate from photon-counting noise, pixelation noise, and background noise [33–36] have been shown to induce a bias in the determination of the power-law (or anomalous) exponent [37]. This effect cannot be fully resolved by an improved ensemble average or a longer experiment [38,39]. For the case of the PDF of the duration of interevents or states, the experimental errors hinder the determination of the state in which the system is. Thus, a minimal number of successive measurements is required to assign a state to the system. Furthermore, the duration of the experiments itself affects the observed PDF: it is usually treated using an upper truncated Pareto distribution and has been applied in different contexts, e.g., in finance [40–42], geology [43], and biology [32,44]. In the current work, we establish a mathematical framework to formulate the distribution of an observed time series under these two constraints, providing the mathematical relation between the original PDF of the duration of the states and the observed PDF.

The organization of the paper is in the following. In Sec. II, we define the three distinct dynamic models (Fig. 1) under consideration and establish our mathematical framework. In Sec. II A, we construct a theory to deal with the temporal-spatial resolution effect. In Sec. II B, we investigate the modification of event time PDFs due to the effect of a finite observation window. Thereafter, in Sec. II C we combine the two effects, constructing the complete theory for accessing the event time PDF under the limits of the resolution and finite observation time window. For each case, we derive a formal relation of the observed PDF of the duration of events and give an analytical expression for the special case of the power-law distribution. For confirming the pertinence of our theory, we also perform simulations of the CTRW and LW models and fit the distribution of the duration of events with these analytical expressions. In Sec. III, we apply our theory to an experimental case: the transport of mRNA-protein (mRNP) particles along dendrites in neuronal cells. We extract the power-law exponent of the distribution of the duration of the immobile state of these macromolecular complexes and discuss the results therein. Finally, we give some concluding remarks.

II. THEORY

The underlying process we consider is a two-state process (state S and state S'): a particle alternates between one state to the other with a duration drawn from a given PDF $\psi_S(t)$ [resp. $\psi_{S'}(t)$] or with a given rate. Representative examples include time series of events, such as earthquake occurrence or arrival of emails [Fig. 1(a)], and on-off processes like blinking of quantum dots [45]. In the diffusion process, the continuous-time random walk is a typical example. In the

framework of CTRW, a random walk is described by instantaneous jumps and waiting events in between the successive jumps [Fig. 1(b)]. An additional important example is a LW with rests [Fig. 1(c)]. In this process, the instantaneous jump in the (subdiffusive) CTRW is replaced by a ballistic run whose duration time is proportional to the jump length. The process is thus understood as ballistic diffusion alternating with immobile motions. The statistical property of the PDF of the duration time of each state is a fundamental characteristic of the process.

In practice, the time series data consist of a succession of positions measured every time interval Δt. Therefore, the data set is given by $\mathcal{X} = \{X_i, i = 0 \ldots N\}$ where i is the time index and N is the maximum number of measurement. A conventional method to identify the state is to calculate the instantaneous velocity $v_{i,\text{inst}} = \frac{X_{i+1}-X_i}{\Delta t}$. If the instantaneous velocity is below a given threshold, the particle is in an immobile state and is in a mobile state otherwise. This strategy is a projection from the position to the state of the system, and it generates a time series $\{S_i, i = 1 \ldots N-1\}$ where S_i is the state at time $i\Delta t$. In general, there exist other complicated strategies identifying the system state [46–48], but they all consist of a projection $\mathcal{F}$ from the data set $\mathcal{X}$ and result in a time series of states $\mathcal{S} = \mathcal{F}(\mathcal{X}) = \{S_i, i = 1 \ldots N-r\}$ where r is the minimum data points needed to determine the state of the system. Once $\mathcal{S}$ is obtained, the duration time of each state and their observed PDFs are immediately extracted from it. Using the analytical theory and computer simulations, we demonstrate that the original PDFs of the duration of each state are different from the observed PDFs. The mathematical relation between the two PDFs is obtained in terms of the aforementioned resolution r and the maximal observation time of the time series.

A. Temporal-spatial resolution

In this section, we investigate the sole effect of the resolution over the observed PDFs. As stated before, determining the state $\{S_i\}$ requires a minimum number of data points. If one uses the instantaneous velocity aforementioned, it only requires two data points. However, in general it requires more data points because of the noise or of the measurement errors. These minimum data points are the resolution r. In other words, with the knowledge of r data points, we determine the system state. However, in doing so we have implicitly assumed that the state remains unchanged during $r\Delta t$, which is not generally true. There exists a possibility that a change of state occurs during the time interval of $r\Delta t$.

In Figs. 2(a)–2(c), we give schematics of the measurement process and show the consequences of the resolution over the measured trajectory against the real one. In Fig. 2(a), we consider a time series of events. The measurement occurs every time step Δt; therefore, if two events occur within that time step only one event is detected. Thus the statistics of interevents is modified because of the inability to measure the interevent duration shorter than Δt. In Figs. 2(b) and 2(c), we show how the resolution modifies the real trajectory for the cases of CTRW and LW with rests. Suppose a trajectory such that the system stays in an immobile state for t_1, undergoes an event (jump or ballistic motion) and then again remains in the immobile state for t_2. If the event induces a change in the trajectory lower than the resolution Δx or Δt, the change is not detected. Therefore, on the measured trajectory, only a single event is recorded which last $t_1' > t_1$. Note that the resolution is related to a physical limitation (e.g., camera resolution) and we will make use of it to evaluate the probability of errors. These errors modify the waiting time PDF and we illustrate in Figs. 2(d) and 2(g) the effects of it for the case of a CTRW with power-law waiting times PDF; in each plot we show the original PDFs (solid line) from which the CTRW was generated and the observed PDFs (symbols) obtained after measuring and identifying the immobile state. In the following, we will derive in detail the exact relation between them. Suppose that we have observed that the state S of the system lasts for a certain period of time t. There is a probability P_r that during the observation time $t(>0)$ the state has quickly changed to S' during a time interval shorter than $r\Delta t$ at time $\tau_1(<t)$ and come back to S. Generalizing this idea, there is a probability $(P_r)^m$ that during the observation time t the state has briefly changed m times to S' for a time period shorter than $r\Delta t$. Assuming that the duration of the state S' is infinitesimal (as usually considered in the time series of the event occurrence and CTRWs in Fig. 1), the apparent PDF of duration time of the state S can be written in terms of the true PDF $\psi_S(t)$ and P_r as in the following:

$$\psi_{\text{reso},S}(t) = \frac{1}{\mathcal{N}}\Bigg[\psi_S(t) + P_r \int_0^t \mathrm{d}\tau_1 \psi_S(\tau_1)\psi_S(t-\tau_1) + {P_r}^2 \int_0^t d\tau_1 \psi_S(\tau_1) \int_{\tau_1}^t d\tau_2 \psi_S(\tau_2 - \tau_1)\psi_S(t-\tau_2) + \ldots\Bigg]. \tag{2}$$

On the right-hand side, the first term takes into account the probability that the state S lasts continuously up to time t, the second term that the state S changes briefly to S' at time τ_1, the third that the state S changes briefly to S' two times at τ_1 and τ_2, etc.

Because P_r is the probability that the state lasts for a period of time shorter than the resolution $r\Delta t$, it depends on which underlying process is considered. For the CTRW, it is the probability that a jump is smaller than the spatial resolution $r\Delta x$

$$P_r = \int_0^{r\Delta x} dx\, \psi_{\text{jump}}(x), \tag{3}$$

where $\psi_{\text{jump}}(x)$ is the jump length PDF. For the LW with rests [Fig. 1(c)], it is the probability that the run is shorter than the temporal resolution

$$P_r = \int_0^{r\Delta t} d\tau\, \psi_{S'}(\tau), \tag{4}$$

where $\psi_{S'}(\tau)$ is the PDF of duration time of run events (S'). Thus, P_r is related to the cumulative distribution of the S' state.

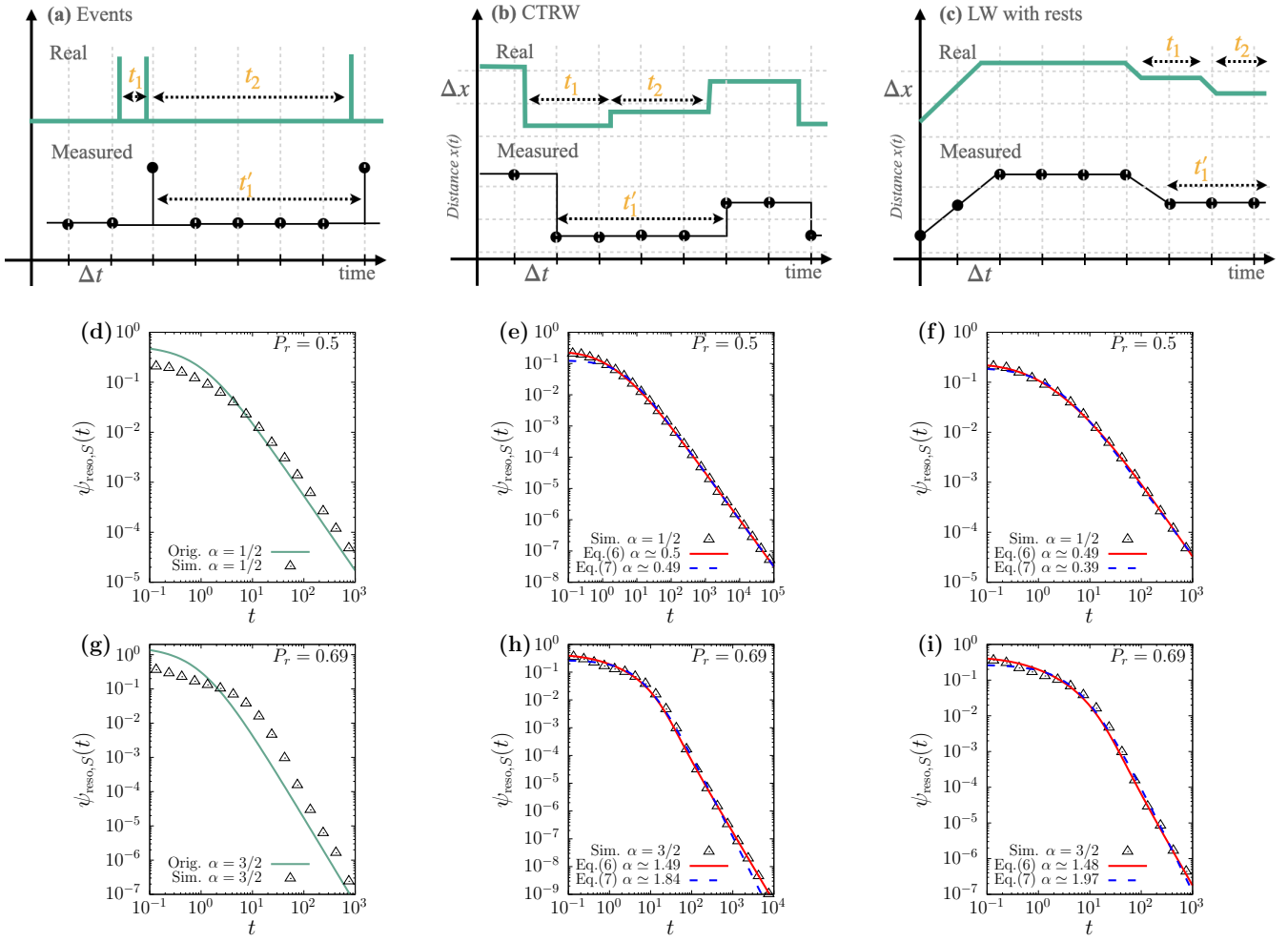

FIG. 2. Top: The schematics of the measurement process for (a) a time series of events, (b) a CTRW process, and (c) a LW with rests. If a change occurs within the time resolution Δt and/or the spatial resolution Δx, the event is undetected. Because of this effect, the statistics of interevent times (or waiting times) can be altered substantially. In the panels (a)–(c), we schematically draw the original time sequences of events (upper) and the recorded time sequences under the resolution limit (bottom). Middle and bottom: Plots of the observed waiting time PDFs of the CTRW process (b) with a power-law distributed waiting time (7) and an exponentially distributed jump length $\psi_{\text{jump}}(x) \sim e^{-x/x_0}$. All the plots display the waiting time PDFs for two power-law exponents α: the set of three plots on the middle line is for $\alpha = 1/2$ and the set on the bottom line is for $\alpha = 3/2$. The left panels (d) and (g) illustrate how different are the original PDFs $\psi_S(t)$ (solid lines) used to generate the CTRW trajectories and the observed PDFs $\psi_{\text{reso},S}(t)$ (symbols) obtained from the measured trajectory. The simulation data [(e), (f), (h), (i)] were fitted with our theory Eq. (6) using the numerical inverse Laplace transform (solid lines) and with the original power-law PDF (7) used in the simulation (dashed lines). Here, the error bars of the simulation data are smaller than the symbol size. The corresponding best-fit curve and the fit values are shown in the plots and are in excellent agreement with the simulations even though the probability of error P_r is high, as in the (h) and (i) panels. When the fitting range of the (e) and (h) panels is reduced to (f) and (i), the fitting exponent using a regular power-law distribution Eq. (7) worsens. However, the fitting exponent using our theory Eq. (6) remains correct irrespective of the fitting range. The following are the parameters used in the simulation: (d), (e), (f): $\alpha = 1/2$, $\tau_0 = 1$, $x_0 = 1.44$, and $r\Delta x = 1$ ($P_r = 0.5$). (f), (g): $\alpha = 3/2$, $\tau_0 = 1$, $x_0 = 1.71$, and $r\Delta x = 2$ ($P_r = 0.69$).

Using a Laplace transform $\hat{f}(s) = \mathcal{L}[f(t)] = \int_0^\infty dt\, f(t)e^{-st}$, we rewrite Eq. (2) as

$$\hat{\psi}_{\text{reso},S}(s) = \frac{1}{\mathcal{N}}\left[\hat{\psi}_S(s) + P_r\hat{\psi}_S(s)^2 + P_r^2\hat{\psi}_S(s)^3 + \dots\right] = \frac{1}{\mathcal{N}}\sum_{n=0}^{\infty} P_r^n\hat{\psi}_S(s)^{n+1}. \tag{5}$$

Because $\psi_S(t)$ is a probability distribution, it ensures $\hat{\psi}_S(s = 0) = 1$ and the normalization factor $\mathcal{N}$ is $\mathcal{N} = \frac{1}{1-P_r}$. The above geometric series then leads to

$$\hat{\psi}_{\text{reso},S}(s) = \frac{(1-P_r)\hat{\psi}_S(s)}{1 - P_r\hat{\psi}_S(s)}. \tag{6}$$

Analytically, we obtain the formal expression for the apparent PDF such that $\psi_{\text{reso},S}(t) = \mathcal{L}^{-1}[\hat{\psi}_{\text{reso},S}(s)]$. Although performing the inverse Laplace transform is generally not feasible, we are able to evaluate it numerically with the Gaver-Stehfest algorithm [50] that has been proven to converge exponentially fast if the function is analytic around the

point of evaluation [51]. Then, Eq. (6) can be used to fit the data and infer the parameters of the original PDF $\psi_S(t)$. Equation (6) is valid for any alternating process; therefore it can be applied to any distributions $\psi_S(t)$.

To investigate the effect of the temporal-spatial resolution, let us consider a normalized power-law PDF

$$\psi_S(t) = \frac{\alpha \tau_0^\alpha}{(t+\tau_0)^{1+\alpha}} \tag{7}$$

and numerically obtain the event statistics limited by a given resolution. Before the numerical study, we discuss the asymptotic behaviors of $\psi_{\mathrm{reso},S}(t)$ at the two limiting conditions of $t \to 0$ and $t \to \infty$ by the virtue of the Tauberian theorems: (1) The information of $\psi_{\mathrm{reso},S}(t \to 0)$ is obtained via $\lim_{s\to\infty} \hat{\psi}_{\mathrm{reso},S}(s) = \frac{\alpha(1-P_r)}{s}$, which gives the relation

$$\psi_{\mathrm{reso},S}(0) = (1-P_r)\psi_S(0). \tag{8}$$

(2) For the large-time limit and with $\tau_0 = 1$, we find that $\hat{\psi}_{\mathrm{reso},S}(s \to 0) \simeq 1 - \frac{\alpha s^\alpha}{1-P_r}$, which translates into the time domain

$$\psi_{\mathrm{reso},S}(t) \sim \frac{1}{(1-P_r)t^{1+\alpha}}. \tag{9}$$

These two limiting behaviors are the illustration of the effects of measurements on the real trajectory: it captures the probability to fail to detect a change of states and, therefore, to merge two short consecutive events into a longer single one. In Figs. 2(d) and 2(g), we clearly see these effects. As $\lim_{t\to\infty} \psi_{\mathrm{reso},S}(t) > \lim_{t\to\infty} \psi_S(t)$, this means that the short-duration events are likely to aggregate into longer events. Oppositely, as $\psi_{\mathrm{reso},S}(0) < \psi_S(0)$, the short-duration events are also less likely to be the results of aggregation themselves. The result Eq. (9) also suggests that if it is possible to observe a time series within a sufficiently long observation time ($t \to \infty$) one can obtain the power-law exponent of the original PDF by measuring the long-time behavior even under the temporal-spatial resolution limit with a decreased amplitude by the factor of $1 - P_r$. However, if a time series is not sufficiently long, estimating α by means of the original PDF (7) often results in an incorrect value, which is tested below.

In Figs. 2(d)–2(i), we simulated CTRW processes with a power-law distributed waiting time PDF (7) for $\alpha = 1/2$ ($P_r = 0.5$) and $\alpha = 3/2$ ($P_r = 0.69$) and for several observation times. Figures 2(d)–2(f) show the observed PDFs $\psi_{\mathrm{reso},S}(t)$ from the simulation (upper triangle) and two fitted PDFs, one from our theory Eq. (6) (solid red line) and the other one from the original PDF (7) (dashed blue line). In Fig. 2(e), as the fitting range is six decades long $[10^{-1}, 10^5]$, both fittings correctly estimate the input value of α. However, simply narrowing the fitting range to four decades long $[10^{-1}, 10^3]$, the power-law fitting Eq. (7), while visually agreeable with the simulations, fails to correctly infer the α [Fig. 2(f)]. A similar observation can be made in Figs. 2(g)–2(i) for the case of $\alpha = 3/2$ as reducing the fitting range for the power-law fitting Eq. (7) worsens the estimate of α even though it seemingly explains well the data. Meanwhile, we confirm that the estimated values of α with our theory Eq. (6) are in good agreement with the input value regardless of the observation window t of the data and regardless of the resolution value.

Note that the fitting range dependence for the simple power-law (7) is a consequence of the asymptotic behavior Eq. (9) of our theoretical result Eq. (6): as the upper boundary of fitting range increases, the behavior of the distribution Eq. (6) tends to the regular power law (7). Therefore, for an infinitely long fitting range, both fittings will give the same estimate of α because the resolution only affects the short-argument behavior. For any other cases, the fitting with the regular power law (7) will depend on the choice of the fitting range; it is known as a major difficulty to properly identify the range of power law [11]. However, our result suggests that if the breakage of the power-law behavior is solely due to the resolution, we no longer need to identify this power-law fitting range and the distribution Eq. (6) can be used over the entire range of data.

B. Time window

Here, we examine how the original PDFs are modified by the sole effect of the time window. By analyzing how the duration of a state is recorded during an experiment, we establish the relation between the original and observed PDFs of state duration.

To measure the duration time of a state S, an event has to occur within the time window $[0, T]$ of the experiment. Thus, the time window will strongly affect the measured PDF as no event longer than the time window itself will be registered; when a duration time PDF has a characteristic timescale such as an exponential distribution, a proper choice of the time window could constitute a solution. However, if tuning a time window is not possible or if the PDF has no characteristic timescale as for power-law distributions, the time-window effect has to be taken into account explicitly.

In Fig. 3(a), we schematically depict the typical situation to be considered. Assume that during our observation in $[0, T]$ an event occurs at time τ with a probability $P(\tau)$. This event will last for a duration t distributed according to $\psi_S(t)$ [or $\psi_{S'}(t)$]. If $t + \tau$ is larger than the time window T, then it cannot be registered in the statistics. For a given time τ for an event to start, the probability of observing the complete event is $\mathrm{Prob}(t < T - \tau) = \int_0^{T-\tau} du\, \psi_S(u)$. Therefore, each event registered in the distribution will be weighted by this probability

$$\psi_{\mathrm{time},S}(t) = \frac{\psi_S(t)}{\mathcal{N}} \int_0^{T-t} d\tau\, P(\tau) \int_0^{T-\tau} du\, \psi_S(u)\Theta(T-t), \tag{10}$$

where the step function $\Theta(T - t)$ ensures $t < T$. The mathematical expression (10) is applied to any time series regardless of the exact form of the distribution $\psi_S(t)$ and the probability $P(\tau)$. Assuming the process is almost time-translation invariant, the probability $P(\tau)$ becomes a constant, absorbed into the normalization. This is typically the case in Lévy walks when the aging time becomes large enough [52]. Evaluating the integrals for the power-law case Eq. (7) [53], we obtain for $t \in [0, T]$

$$\begin{aligned}\psi_{\mathrm{time},S}(t) &= \frac{\psi_S(t)}{\mathcal{N}}\left[T - t + \tau_0^\alpha \frac{(T+\tau_0)^{1-\alpha} - (t+\tau_0)^{1-\alpha}}{\alpha - 1}\right] \\ &= W(t,T)\psi_S(t).\end{aligned} \tag{11}$$

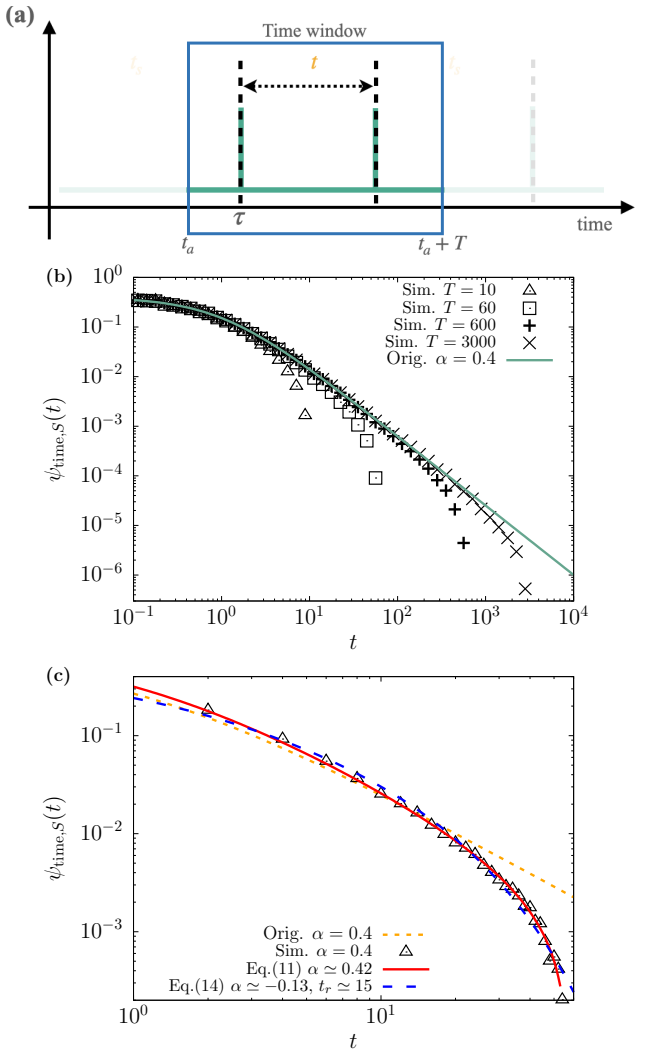

FIG. 3. (a) Scheme of a typical experiment: t_a represents the beginning of the experiment where the measurements start. T is the duration of the experiment. An event occurs at a random time τ followed by another event at time $\tau + t$. The interevent time t is drawn from a given distribution $\psi_S(t)$. (b) The observed PDFs of waiting times from the CTRW processes with a power-law distributed waiting time with $\alpha = 0.4$. The solid line is the original power-law distribution $\psi_S(t)$ used to generate trajectories. The symbols are the distribution observed through different window sizes $\psi_{\text{time},S}(t)$. The normalization is such that $\psi_S(0) = \psi_{\text{time},S}(0)$. (c) The original PDF (orange dashed line) of the process we simulated is displayed with the observed waiting time PDF of a CTRW process recorded within a finite observation time window T. The data from simulations (symbols) is compared with the fit by our theory (solid line) Eq. (11) of $\psi_{\text{time},S}(t)$ with $\tau_0 = 1$ and by an exponentially truncated power law Eq. (14) (dashed line). The CTRW was simulated with the waiting time PDF (7) with $\alpha = 0.4$ and $\tau_0 = 1$. The observation time window was $T = 60$. Even though the exponentially truncated power law Eq. (14) gives visually a reasonable fit, it fails to capture the correct exponent. However, the fit based on our theory Eq. (11) displays an excellent agreement with the simulations and recovers the correct exponent.

We note that, contrary to a naive expectation, $\psi_{\text{time},S}(t)$ is not an exponentially truncated power law which might behave as $\psi_{\text{time},S}(t) \simeq \exp(-C \times t/T)\psi_S(t)$. The truncation factor behaves as

$$W(t,T) \simeq \frac{1}{\mathcal{N}}\left[\left(T + \frac{(T+1)^{1-\alpha}\tau_0^\alpha - \tau_0}{\alpha - 1}\right) - \frac{\alpha}{2\tau_0}t^2\right] \quad (12)$$

when t is small. This means that $\psi_{\text{time},S}(t) \propto \psi_S(t)$ up to a prefactor. When $t \to T$, the truncation factor is approximated to

$$W(t,T) \simeq \frac{1}{\mathcal{N}}\left[1 - \frac{\tau_0^\alpha}{(T+\tau_0)^\alpha}\right](T-t). \quad (13)$$

That is, the truncation by the finite observation time T is not an exponential cutoff but a linear decay with $T - t$.

In Figs. 3(b) and 3(c), we test our theory with simulations of a CTRW process with power-law distributed waiting times with the exponent $\alpha = 0.4$. We record the events that happened during the time window $[0, T]$ and we plot the observed waiting times PDF (symbols). In Fig. 3(b), we plot the observed waiting time PDF for increasing the time window T, along with the original distribution. It clearly displays the effect of the cutoff on the waiting time PDF; as T is larger, the observed PDF gets closer to the original PDF. In Fig. 3(c), we also infer the value of α from the observed data using our theoretical expression Eq. (11) and using an exponentially truncated power law

$$\psi_{\text{ETPL}}(t) = \frac{t_r^\alpha}{\Gamma\left(-\alpha, \frac{t_{\min}+1}{t_r}\right) - \Gamma\left(-\alpha, \frac{T+1}{t_r}\right)} \frac{e^{-(t+1)/t_r}}{(t+1)^{1+\alpha}}. \quad (14)$$

Here, $\psi_{\text{ETPL}}(t)$ is normalized for $t \in [t_{\min}, T]$. While apparently both fits explain well the simulation data, the extracted value of α is very different. We confirm that our theory Eq. (11) correctly recovers the original exponent. However, the empirical approach with the exponentially truncated power law produces an unrealistic estimation for α, which was $\alpha = -0.13$ and a cutoff time $t_r = 15$.

To sum up, when looking for a power-law behavior in data from any experiments with a definite time window, Eq. (11) should be used instead of the regular power law (7).

C. The combined effects of the resolution and time window

Based on our theoretical studies in Sec. II A and II B, here we seek to find the expression of the observed PDF $\psi_{\text{obs},S}(t)$ limited by the resolution and time window simultaneously. Combining the two main results Eq. (6) and Eq. (10), we find that $\psi_{\text{obs},S}(t)$ satisfies the following formal expression

$$\psi_{\text{obs},S}(t) = \frac{\psi_{\text{reso},S}(t)}{\mathcal{N}} \int_0^{T-t} d\tau\, P(\tau) \int_0^{T-\tau} du\, \psi_{\text{reso},S}(u), \quad (15)$$

where $\psi_{\text{reso},S}(t)$ is the inverse Laplace transform of the function given in Eq. (6). Unfortunately, it is almost infeasible to

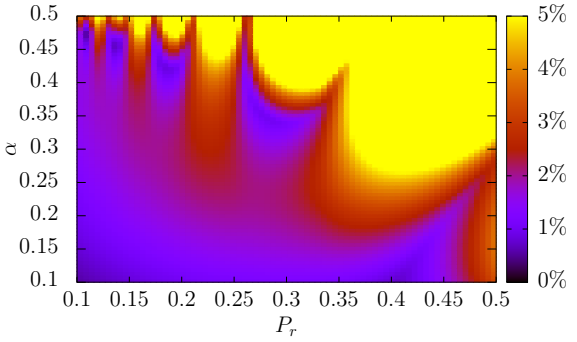

FIG. 4. Maximum of the relative error of the approximation Eq. (16) with respect to the numerical inverse Laplace transform of Eq. (6) for $t \in [1, 100]$. The approximation Eq. (16) can be considered reasonable in the lower left diagonal part, when $\alpha + P_r \lesssim 0.65$.

obtain the analytic expression of $\psi_{\mathrm{reso},S}(t)$ for a power-law PDF. Therefore, we have to proceed with an analytical approximation of $\psi_{\mathrm{reso},S}(t)$ to evaluate Eq. (15) or conduct numerical evaluations of Eq. (15) to get $\psi_{\mathrm{obs},S}(t)$.

Let us first proceed in the former method. For the two extreme limits ($t \to 0$ and $t \to \infty$), we can separately find the analytic expression of $\psi_{\mathrm{reso},S}(t)$ for a power-law PDF (7) with $\tau_0 = 1$. By empirically matching the two limiting results, we end up with the following approximation of $\psi_{\mathrm{reso},S}(t)$:

$$\begin{aligned}\overline{\psi}_{\mathrm{reso},S}(t) \simeq{}& \frac{\psi_S(t)}{1-P_r} + \frac{\alpha(1-P_r) - \frac{\psi_S(0)}{(1-P_r)}}{(t+1)^{2+\alpha P_r}} \\ &+ \sum_{n=2}^{[1/\alpha]} \frac{\alpha^n \Gamma(-\alpha)^n P_r^{n-1}}{(1-P_r)^n \Gamma(-n\alpha)} \\ &\times \left(\frac{1}{(t+1)^{1+n\alpha}} - \frac{1}{(t+1)^{2+\alpha P_r}} \right) \\ &+ \frac{2P_r \alpha \Gamma(-\alpha)}{(1-P_r)^2 (1-\alpha)\Gamma(-\alpha-1)} \\ &\times \left(\frac{1}{(t+1)^{2+\alpha}} - \frac{1}{(t+1)^{2+\alpha P_r}} \right). \end{aligned} \tag{16}$$

Considering that the approximation is valid if the relative error $\frac{|\psi_{\mathrm{reso},S}(t) - \overline{\psi}_{\mathrm{reso},S}(t))|}{\psi_{\mathrm{reso},S}(t)} < 5\%$, we estimate that the domain of validity is such that $P_r + \alpha \simeq 0.65$. In Fig. 4, we plotted the maximum of the relative error of the approximation Eq. (16) in the domain $t \in [1, 100]$ with respect to the numerical inverse Laplace transform of Eq. (6). The heat map is plotted such that the color displayed is yellow when the relative error is >5%. Therefore, all the remaining area corresponds to the case that the approximation is considered valid. We note that the approximation Eq. (16) consists of a sum of power-law terms; therefore replacing each power law by its corresponding expression Eq. (11), we obtain the final approximated expression for the combined effects $\psi_{\mathrm{obs,app}}$ given in Eq. (B4) in Appendix B.

Alternatively, we can obtain $\psi_{\mathrm{obs},S}(t)$ by numerically evaluating the formal expression Eq. (15). For this, we rewrite the integral expression in Eq. (15) as

$$\begin{aligned}\psi_{\mathrm{obs},S}(t) = {}& \frac{\mathcal{L}^{-1}[\hat{\psi}_{\mathrm{reso},S}](t)}{\mathcal{N}} \\ &\times \left(\mathcal{L}^{-1}\left[\frac{\hat{\psi}_{\mathrm{reso},S}}{s^2} \right](T) - \mathcal{L}^{-1}\left[\frac{\hat{\psi}_{\mathrm{reso},S}}{s^2} \right](t) \right). \end{aligned} \tag{17}$$

We then use the Gaver-Stehfest algorithm [50] to evaluate the inverse Laplace transform in the above expression numerically. We note here that the validity of Eq. (15) is not restricted to a power-law distribution and can be used with any distribution.

We test our theory with an example of Lévy walk with rests schematically explained in Fig. 1(c), which will be our dynamic model in the next section for the application of the developed theories to an experimental system. The simulated process and its event time PDFs can be understood as those of a CTRW process with the P_r defined in Eq. (3). In Fig. 5, we simulate a Lévy walk with rests where the run (ballistic phase) event is generated with random sojourn times governed by a truncated power law and the rest event with random waiting times governed by a power-law PDF. For further information, see Appendix A for the simulation detail. Here, we extract the (power-law) rest time PDFs from the simulated trajectories in the presence of the resolution and time-window limits.

Shown in Fig. 5 are the observed rest time PDFs of the Lévy walk process for two distinct parameter cases. To infer the power-law exponent α we fit the simulation data with the following three theoretical expressions (S = "rest"): (i) the expected PDF $\psi_{\mathrm{obs},S}(t)$ based on the exact theory Eq. (17),

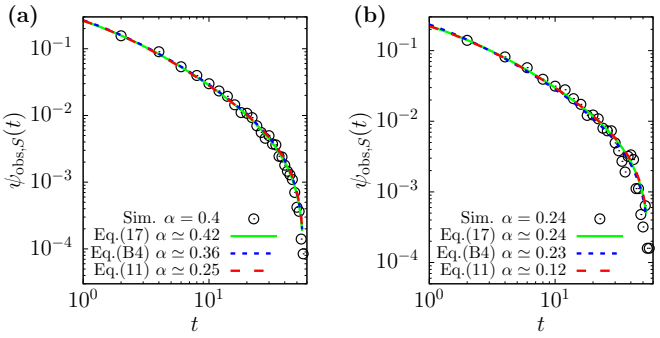

FIG. 5. The observed waiting time PDF of rest events in the model of a Lévy walk with rests [Fig. 1(c)] under the limitation of the resolution and time window. The Lévy walk process is generated with an exponentially truncated power-law PDF of run times $\psi_{\mathrm{run}}(t) \propto \frac{e^{-t/t_r}}{(t+1)^{1+\eta}}$ and a power-law PDF of rest times $\psi_{\mathrm{rest}}(t)$ given by Eq. (7). See the schematic of this process in Fig. 1(c). The simulation parameters are (a) $\eta = 0.1$, $t_r = 20$, $\alpha = 0.4$, and $r\Delta t = 1$; (b) $\eta = 0.4$, $t_r = 20$, $\alpha = 0.24$, and $r\Delta t = 0.6$. In both panels, the symbols represent the simulations results. The solid line shows the fit using our exact theory Eq. (17) while the dotted line is the fit using the approximated PDF, $\overline{\psi}_{\mathrm{obs},S}(t)$, from Eq. (B4). The dashed line represents the fit using $\psi_{\mathrm{time},S}(t)$ [Eq. (11)] that incorporates the effect of the time window in the absence of the resolution limitation. While all the fit curves seemingly show good agreement with the simulations, only the one based on our complete theory Eq. (17) gives the correct exponent.

(ii) the approximated PDF $\overline{\psi}_{\mathrm{obs},S}(t)$ via Eq. (B4), and (iii) $\psi_{\mathrm{time},S}(t)$ based on Eq. (11), which is the theoretical PDF that only takes into account the effect of time window. The results show that although the data seem to be fitted well with the three expressions the fitting values greatly differ. It is demonstrated that the exact expression (i) estimates the underlying exponent successfully for the two data set [(a) and (b)] even though the observation time window is not sufficiently long. Using the approximated PDF $\overline{\psi}_{\mathrm{obs},S}(t)$, we can infer α in good agreement with the ground true value when the resolution is high (i.e., r is small) [Fig. 5(b)]. However, the estimation becomes inaccurate when the resolution is low (i.e., r is small) [Fig. 5(a)]. Finally, we confirm that without incorporating the resolution effect the PDF $\psi_{\mathrm{time},S}(t)$ fails the correct estimation of the power-law exponent. Thus, Eq. (17) is the pinnacle of this study as it encompasses the two main constraints of experiments and gives us how a distribution is transformed when subjected to these constraints.

III. AN EXPERIMENTAL APPLICATION: THE TRANSPORT OF mRNP PARTICLES IN NEURONAL CELLS

As an experimental application of our theory, we determined the statistics of the dynamics of β-actin mRNP complexes transported along the dendrites of neurons by motor proteins [Fig. 6(a)]. Previously, we have shown that the motion of β-actin mRNP complexes consists of an alternation of rests and runs. See the kymograph of mRNP particles in Fig. 6(b). We performed experiments following a similar protocol used in [10] except for the use of bicuculline for neuronal stimulation. Briefly, we cultured hippocampal neurons from the MCP×MBS mice [54], in which every single endogenous β-actin mRNA is labeled with multiple green fluorescent proteins. At 12–15 days *in vitro*, we stimulated the neurons by treating them with 50 μM bicuculline for 20 min. At 40–60 min after the onset of the stimulation, we imaged the movement of individual β-actin mRNP particles in proximal dendrites (0–50 μm from the cell body) at 200 ms intervals over a one-minute time course. Being fluorescently labeled, the individual mRNPs appear as bright spots in Fig. 6(a). Kymographs of the time-lapse images were generated, from which the positions of fluorescently labeled mRNPs were detected and registered; see Fig. 6(b).

As observed in the kymograph, the stochastic diffusion dynamics of single mRNP particles are described by the Lévy walk with rests introduced in Fig. 1(c). The motion of mRNPs is an alternating dynamics of the run and rest phases. Here, the run is a ballistic movement with random sojourn times while the rest is the stop state with waiting times governed by a PDF distinct from the run's. After the identification of the trajectories $\{X_i, i = 0 \ldots N\}$ from the kymographs, we proceeded to the determination of their states. For this, we calculated the velocity $\frac{X_{i+1}-X_i}{\Delta t}$ where $\Delta t = 0.2$ s was the time interval of imaging. After averaging and filtering this velocity profile, we determined the dynamic state of the mRNP particle by applying the following criterion: if the velocity was $< v_{\mathrm{threshold}} = 0.3$ μm/s then the particle was considered in a rest state; if not it was considered in a run.

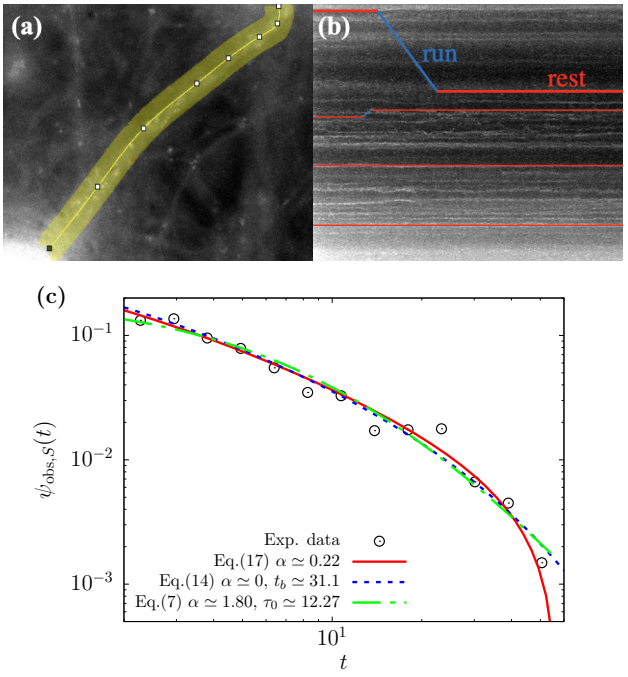

FIG. 6. (a) Live-cell image of a hippocampal neuron showing fluorescently labeled β-actin mRNPs. Images were taken every time interval $\Delta t = 200$ ms. (b) A typical kymograph for an ensemble of mRNP particles spotted along an observed dendrite as in (a). The single mRNP motion is composed of run and rest phases, which are marked in blue and red colors, respectively. (c) Distribution of the duration of rest events $\psi_{\mathrm{rest}}(t)$. Symbols: Experimental PDF. Solid line: The best fit using our theory Eq. (17) with $\alpha \approx 0.22$. The resolution has been estimated to be such that $P_r \simeq 0.45$. Dashed line: The best fit using an ETPL Eq. (14) with an additional constraint of $\alpha > 0$ results in $\alpha \approx 0$ and $t_b \approx 31.1$ s. Dashed-dotted line: The best fit using a simple power law Eq. (7) with $\alpha \approx 1.80$ and $\tau_0 \approx 12.27$. The power-law function was normalized to unity on the range of the plot.

We now focus on the PDF ψ_{rest} of the waiting time of the rest event. For the run event, it was shown that the sojourn time PDF was not of a power law [10], which was explained well by an exponentially truncated power law $\psi_{\mathrm{run}}(t) \sim \frac{e^{-t/t_r}}{(t+1)^{1+\eta}}$ with $\eta = 0.52$ and $t_r = 12.5$ s. Using this information, we calculated the probability P_r that a run is too short to be detected. Estimating that the resolution is about $n_{\min} = 5$ data points or about 1 s (see Appendix C), this gives $P_r = \int_0^{n_{\min}\Delta t} \psi_{\mathrm{run}}(t)\,dt = 1 - \frac{\Gamma(-\eta,(n_{\min}\Delta t+1)/t_r)}{\Gamma(-\eta,1/t_r)} \simeq 0.45$.

In Fig. 6 we plot the rest time PDF from our experiment. We infer the power-law exponent α of the PDF from the data with $\psi_{\mathrm{obs},S}(t)$ that takes into account the combined effects of the resolution and time window [Eq. (17)]. For comparison, we also measure the best-fit values of α with power-law PDFs, Eq. (14) (exponentially truncated power law) and Eq. (7) (power law). We find that the fit with the single power law results in $\alpha \approx 1.8$, while the fit with the exponentially truncated power law (ETPL) with the constraint $\alpha > 0$ gives $\alpha \approx 0$ and the truncation characteristic time $t_b = 31.1$ s. Although the experimental data are well explained, at least visually, by both fit curves, the two reference methods give inconsistent values for

α. Moreover, neither of them turns out to be physically correct in that the β-actin mRNP's motion follows an aged Lévy walk from our previous study [10]. Namely, the Lévy walk with rest events governed by the above ETPL or by a power-law PDF with α (≈ 1.8) >1 cannot age due to the finite first moment of the rest times. Therefore, the fitted exponents α using the two reference power-law PDFs have to be rejected for dynamical reasons. Contrary to these empirical approaches, we obtain $\alpha \approx 0.22$ from our theory based on $\psi_{\mathrm{obs},S}(t)$. The estimated value not only explains well the data over the entire time window (red curve in Fig. 6) but it also satisfies the condition $0 < \alpha < 1$ to be compatible with the reported aging transport dynamics of the β-actin mRNP particle. Note that the fit with our equation (17), albeit a single-parameter fit, outperforms the other ones via Eqs. (14) and (7) that have two fit parameters [55]. We find that $\alpha \approx 0.22$ is smaller than the value $\alpha \approx 0.32$ obtained in the case of nonstimulated neuron experiments [10].

IV. DISCUSSION AND CONCLUSIONS

Throughout this paper, we have demonstrated the necessity to take into account the way data are collected in order to proceed to a meaningful analysis. We have considered two fundamental constraints that are intrinsic to experiments: the spatiotemporal resolution and the time window (or duration). We chose to deal with the constraints in the temporal domain but all the results presented can also be interpreted and used in the spatial domain. Namely, the time-window constraint represents the duration of the experiment but it can also be interpreted as the spatial extension of the experiment. For the resolution, we can view it as a probability of error: if a change or a variation of the signal is below a certain threshold, that change will not be detected. Then the probability that the signal variation is below the threshold is the probability of error. In the experimental example we have investigated (Sec. III), the time window is the duration of the experiment and the temporal resolution is the minimum number of steps required to detect a change of state.

The main results of this paper are recapitulated with the following three equations: (1) Eq. (6) that tells us how the distribution of interevents or state duration times is modified in the presence of measurement errors; (2) Eq. (11) that gives us the distribution of the duration times as a function of the total observation time of the experiment; (3) Eq. (17) that combines the two aforementioned equations and constitutes the central message of the paper: The effects of the experimental constraints cannot be discarded when determining the exponent of the distribution of the state duration time, and we show how to properly take them into account in order to infer the correct power-law exponent.

Although we have demonstrated the application of our theory to a real system in estimating the power-law exponent and the characteristic time of related PDF duration time in Sec. III, let us additionally discuss other examples. In Ref. [45], the blinking of the quantum dots was reviewed. Indeed, under illumination, colloidal nanocrystals exhibit an intermittency in their photoluminescence referred as blinking. To characterize this phenomenon, the photoluminescence is measured at a constant rate and it displays rapid fluctuations between the on and off states, defined as the sustained emission above a certain intensity threshold for the former and below for the latter. For a certain type of blinking called B type, the distribution of duration of the on state or off state is a power law. As the determination of the on state and off state clearly depends on a threshold and the resolution constraint, it could be of interest to use our expression Eq. (6) for the precise estimation of the power-law exponent from the data.

In Ref. [44], the authors studied spontaneous activity cascades called neuronal avalanches in superficial layers of cortex and they characterized the distribution of avalanche sizes. They showed that the PDF follows a power law within a given range but is affected by the spatially windowed recordings and therefore introduced a hard cutoff parameter. However, they found that for upper values of the cutoff, their PDFs with a cutoff deviate from experiments. Using our framework and setting the observation window to the number of electrodes or equivalently the spatial extension of the detection window, one could use Eq. (11) to recover the observed PDF.

We emphasize that our results do not directly apply to the mean-square displacement analysis and the identification and characterization of the anomalous diffusion exponent in Eq. (1). However, in some special cases, one would be able to use our mathematical formalism to estimate the exponent of a given PDF and try to relate it to the anomalous exponent; for example, in the LW process, the power-law exponent γ of the flight time PDF is connected to the anomalous diffusion exponent $\alpha = 3 - \gamma$ if $1 < \gamma < 2$ and $\alpha = 2$ if $0 < \gamma < 1$ [49]. For any other cases, where the anomalous diffusion occurs due to physical mechanisms other than the power-law statistics, such as the strong correlation among displacements and heterogeneity of the environment, measuring the anomalous exponent under experimental errors is completely a different task.

While there are only a few papers that take into account the spatiotemporal window effect on the cumulative distribution function [14,40–42], our work is an in-depth study to derive the expression of the observed PDFs that encompasses the resolution and time-window effects. Therefore, we believe that our theoretical results will substantially improve the identification of power-law distributions in PDFs from experimental data, e.g., as we performed for the PDF of rest duration of the mRNP particles in neuronal cells.

Finally, we emphasize that, even though we have solely presented how the experiments modify the original power laws of a phenomenon or a process, our mathematical framework is general and can be applied to any distribution. The equations (6), (10), and (17) that we obtained from our understanding of the experimental constraints are not restricted to the specific case of the power-law distributions. Indeed, many real-world process statistics are more complex than a single power law [56–58] and our theory can still be applied to such multiple power-law distributions or non-power-law distributions. More generally, any process subjected to these experimental constraints will have its original statistics modified according to our equations, regardless of the exact form of their original distribution.

ACKNOWLEDGMENTS

This work was supported by the National Research Foundation (NRF) of Korea, Grants No. 2020R1I1A1A0107179 (X.D.), No. 2020R1A2C2007285 (H.Y.P.), No. 2017K1A1A2013241, No. 2020R1A2C4002490 and No. 2021R1A6A1A10042944 (J.-H.J.).

APPENDIX A: SIMULATION DETAILS

In Fig. 5, we have simulated the process of a Lévy walk with rests such that the rest time PDF is $\psi_{\rm rest}(t) = \frac{\alpha}{(t+1)^{1+\alpha}}$ and the run time PDF is $\psi_{\rm run}(t) \sim \frac{e^{-t/t_r}}{(t+1)^{1+\eta}}$. It consists of an alternation of run and rest whose respective random durations are drawn from the corresponding PDFs. At time $t = 0$, all trajectories start with a run. The runs are set to be ballistic motions at a constant velocity $v = 1$. The random times governed by the two PDFs are generated using the inverse transform sampling method [59]. We simulated $N = 10^5$ trajectories consisting of points spaced by $\Delta t = 0.2$ within the observation time window $[\tau_a, \tau_a + T]$ where $\tau_a = 100$ and $T = 60$.

Once a trajectory is simulated, it is recorded with a given resolution parameter r in the following way. Let us assume that a Lévy walk with rests is simulated with a variation of event times as schematically illustrated in Fig. 7(a). For every event in the S and S' states, if $t_{\rm event} > r\Delta t$, this state is recognized to occur and the event is recorded with a duration of $t_{\rm event}$. However, if $t_{\rm event} < r\Delta t$ (e.g., in S state), this event fails to be detected. Then, the event (in S state) is recorded as a part of the previous event (in S' state) and, accordingly, the latter state has an increased duration time by $t_{\rm event}$. We repeat the same protocol for the next events, obtaining the recorded trajectory as in Fig. 7(b).

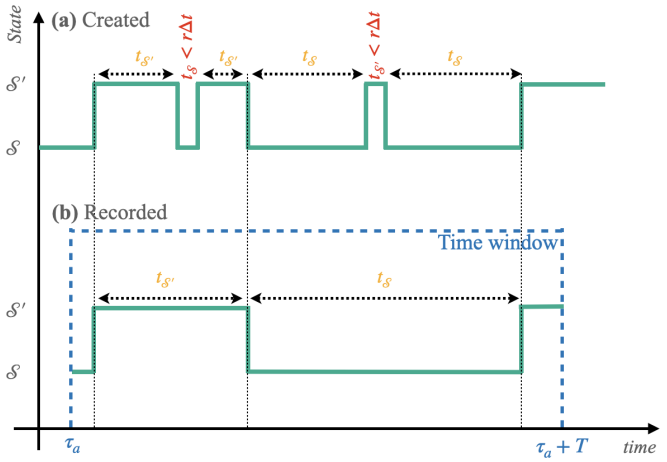

FIG. 7. Example of sampled trajectories. During the sampling, if a duration $t_{S,S'}$ drawn from the corresponding distributions is smaller than $r\Delta t$, the change of event will not appear in the recorded trajectory. (a) The trajectory created before taking care of time window or resolution. (b) The observed or the recorded trajectory

APPENDIX B: DERIVATION OF EQUATION (16)

The expression of Eq. (16) is obtained phenomenologically by matching the initial behavior and the asymptotic behavior of Eq. (6). The series expansion of Eq. (6) gives the large-time behavior

$$\overline{\psi}_{\rm asympt}(t) \simeq \frac{1}{1-P_r}\left(\psi_S(t) + \sum_{n=2}^{[1/\alpha]} \frac{\alpha^n \Gamma(-\alpha)^n P_r^{n-1}}{(1-P_r)^n \Gamma(-n\alpha)} \frac{1}{(t+1)^{1+n\alpha}} + \frac{2P_r \alpha \Gamma(-\alpha)}{(1-P_r)^2(1-\alpha)\Gamma(-\alpha-1)} \frac{1}{(t+1)^{2+\alpha}}\right). \tag{B1}$$

The asymptotic limit of Eq. (6) gives the $t \to 0$ limit

$$\overline{\psi}_{\rm init}(t) = \alpha(1-P_r). \tag{B2}$$

We construct the final expression by requiring that it satisfies both limits and by imposing that it only contains power-law terms

$$\overline{\psi}_{{\rm reso},S}(t) = \overline{\psi}_{\rm asympt}(t) - \frac{\overline{\psi}_{\rm asympt}(0)}{(t+1)^{2+\alpha P_r}} + \frac{\overline{\psi}_{\rm init}(t)}{(t+1)^{2+\alpha P_r}}, \tag{B3}$$

which gives Eq. (16).

To obtain the expression for the combined effects $\overline{\psi}_{{\rm obs},S}(t)$, we replace every simple power law that appears in Eq. (6) by the expression for the time-window effect Eq. (10),

$$\begin{aligned}
\overline{\psi}_{{\rm obs},S}(t) \simeq{}& \frac{\psi_S(t)}{1-P_r}\left[T - t + \frac{(T+1)^{1-\alpha} - (t+1)^{1-\alpha}}{\alpha - 1}\right] + \frac{\alpha(1-P_r) - \frac{\psi_S(0)}{(1-P_r)}}{(t+1)^{2+\alpha P_r}}\left[T - t + \frac{(T+1)^{-\alpha P_r} - (t+1)^{-\alpha P_r}}{\alpha P_r}\right] \\
&+ \sum_{n=2}^{[1/\alpha]} \frac{\alpha^n \Gamma(-\alpha)^n P_r^{n-1}}{(1-P_r)^n \Gamma(-n\alpha)} \frac{1}{(t+1)^{1+n\alpha}}\left[T - t + \frac{(T+1)^{1-n\alpha} - (t+1)^{1-n\alpha}}{n\alpha - 1}\right] \\
&- \sum_{n=2}^{[1/\alpha]} \frac{\alpha^n \Gamma(-\alpha)^n P_r^{n-1}}{(1-P_r)^n \Gamma(-n\alpha)} \frac{1}{(t+1)^{2+\alpha P_r}}\left[T - t + \frac{(T+1)^{-\alpha P_r} - (t+1)^{-\alpha P_r}}{\alpha P_r}\right] \\
&+ \frac{2P_r \alpha \Gamma(-\alpha)}{(1-P_r)^2(1-\alpha)\Gamma(-\alpha-1)} \frac{1}{(t+1)^{2+\alpha}}\left[T - t + \frac{(T+1)^{-\alpha} - (t+1)^{-\alpha}}{\alpha}\right] \\
&- \frac{2P_r \alpha \Gamma(-\alpha)}{(1-P_r)^2(1-\alpha)\Gamma(-\alpha-1)} \frac{1}{(t+1)^{2+\alpha P_r}}\left[T - t + \frac{(T+1)^{-\alpha P_r} - (t+1)^{-\alpha P_r}}{\alpha P_r}\right].
\end{aligned} \tag{B4}$$

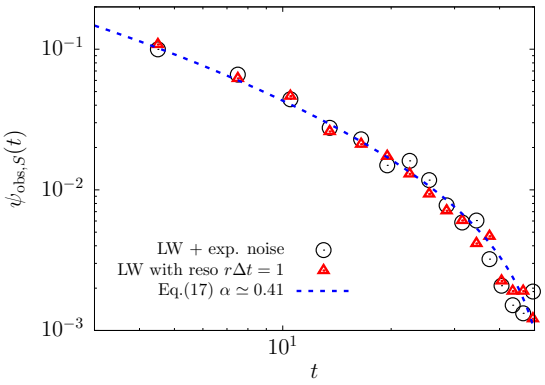

FIG. 8. The PDFs of rest duration extracted from a LW with power law distributed rests over a time window of $T = 60$ (and $\alpha = 0.4$). An experimental noise is added to each computer-generated trajectory and the detection protocol is used to obtain the rest events (black circle). Computer-generated trajectories with the resolution constraint $r\Delta t = 1$ but without an experimental noise (red triangle). Fit of the black circle data with Eq. (17) (dashed blue line).

APPENDIX C: ON THE DETECTION OF RUN AND REST EVENTS FROM THE KYMOGRAPH DATA IN SECTION III

To segregate the runs from the rests, as we stated in the main text, we calculate the instantaneous velocity $v_i = \frac{x_{i+1}-x_i}{\Delta t}$, where $\{x_i\}$ is a recorded trajectory and Δt is the time elapsed between two data points. The velocity profile v_i we obtain from an experiment is noisy and requires a smoothing treatment. We use an edge-preserving nonlinear Gaussian filter [60] called the bilateral filter,

$$\hat{v}_i = \frac{1}{\mathcal{N}} \sum_{j=-6}^{6} v_i G_{\sigma_s}(j) G_{\sigma_v}(|v_{i-j} - v_i|),$$

where $\mathcal{N}$ is the normalization factor, and G_{σ_s} (G_{σ_v}) is a domain (range) Gaussian weight of variance σ_s (σ_v). We iterate this filter until a convergence criteria is satisfied. Then, we identify rest events as the event that continuously satisfies the threshold criteria $\hat{v}_i < v_{\mathrm{threshold}}$. From the previous study [10], it was found that the velocity distribution of the runs displayed a maximum around 1.25 ms^{-1}; therefore we chose $v_{\mathrm{threshold}} = 0.3$ to be as far as possible from the maximum but not too small to avoid capturing fluctuations of the velocity profile.

In order to validate this protocol, we simulate a LW with power-law distributed rests, over a time window $T = 60$, whose exponent is $\alpha = 0.4$. The distribution of the runs is an ETPL with the parameters $\eta = 0.6$ and $t_r = 20$. We add to each trajectory a noise coming from the experimental data set. These noises are actually trajectories that were selected visually because they simply consist of fluctuations around an immobile position. Then, on the noisy trajectories, we apply our protocol to segregate rests and runs. We plot in Fig. 8 the resulting PDF of rest duration (black circle).

We also simulate another LW process with the same parameters but with a resolution of $r\Delta t = 1$ (see Appendix A). We do not add the experimental noise to these trajectories. As the resulting PDF of rest duration (red circle) agrees with the previous one, we consider that the noise and detection protocol can be modeled as a resolution constraint that prevents the detection of events shorter than $r\Delta t = 1$.

Using this resolution parameter, we can estimate the probability of not detecting a run event $P_r \simeq 0.45$ and we fit the PDF from the noisy LW with our theory (dashed blue line). We obtained $\alpha \simeq 0.41$ in excellent agreement with the original value $\alpha = 0.4$ and thus consider the detection protocol valid.

This whole protocol is based on the natural idea that the velocity distinguishes the "immobile" part from the "mobile" ones. The smoothing algorithm we use for the velocity is also common and broadly used, e.g., for image denoising or edge detection, but it requires being tuned specifically for each usage.

[1] L. P. Kadanoff, W. Götze, D. Hamblen, R. Hecht, E. A. S. Lewis, V. V. Palciauskas, M. Rayl, J. Swift, D. Aspnes, and J. Kane, Static phenomena near critical points: Theory and experiment, Rev. Mod. Phys. **39**, 395 (1967).

[2] G. Ahlers, Heat capacity near the superfluid transition in He^4 at saturated vapor pressure, Phys. Rev. A **3**, 696 (1971).

[3] J. A. Lipa, D. R. Swanson, J. A. Nissen, T. C. P. Chui, and U. E. Israelsson, Heat Capacity and Thermal Relaxation of Bulk Helium Very Near the Lambda Point, Phys. Rev. Lett. **76**, 944 (1996).

[4] D. Sornette, *Critical Phenomena in Natural Sciences: Chaos, Fractals, Self-Organization, and Disorder: Concepts and Tools*, 2nd ed., Springer Series in Synergetics (Springer, Berlin, 2004).

[5] P. Bak, C. Tang, and K. Wiesenfeld, Self-organized Criticality: An Explanation of the $1/f$ Noise, Phys. Rev. Lett. **59**, 381 (1987).

[6] A. K. Nekrasova and V. G. Kossobokov, The unified scaling law for earthquakes, J. Volcanolog. Seismol. **14**, 353 (2020).

[7] K. Zhao, M. Musolesi, P. Hui, W. Rao, and S. Tarkoma, Explaining the power-law distribution of human mobility through transportation modality decomposition, Sci. Rep. **5**, 9136 (2015).

[8] A. James, M. J. Plank, and A. M. Edwards, Assessing Lévy walks as models of animal foraging, J. R. Soc. Interface. **8**, 1233 (2011).

[9] K. Chen, B. Wang, and S. Granick, Memoryless self-reinforcing directionality in endosomal active transport within living cells, Nat. Mater. **14**, 589 (2015).

[10] M. S. Song, H. C. Moon, J.-H. Jeon, and H. Y. Park, Neuronal messenger ribonucleoprotein transport follows an aging Lévy walk, Nat. Commun. **9**, 344 (2018).

[11] A. Clauset, C. R. Shalizi, and M. E. J. Newman, Power-law distributions in empirical data, SIAM Rev. **51**, 661 (2009).

[12] M. Perc, The Matthew effect in empirical data, J. R. Soc. Interface. **11**, 20140378 (2014).

[13] A. D. Broido and A. Clauset, Scale-free networks are rare, Nat. Commun. **10**, 1017 (2019).

[14] K. Jonsdottir, M. Lindman, R. Roberts, B. Lund, and R. Bödvarsson, Modelling fundamental waiting time distributions for earthquake sequences, Tectonophysics **424**, 195 (2006).

[15] S. Jin, P. M. Haggie, and A. Verkman, Single-particle tracking of membrane protein diffusion in a potential: Simulation, detection, and application to confined diffusion of CFTR Cl^- channels, Biophys. J. **93**, 1079 (2007).

[16] T. H. Harris, E. J. Banigan, D. A. Christian, C. Konradt, E. D. Tait Wojno, K. Norose, E. H. Wilson, B. John, W. Weninger, A. D. Luster, A. J. Liu, and C. A. Hunter, Generalized Lévy walks and the role of chemokines in migration of effector $CD8^+$T cells, Nature (London) **486**, 545 (2012).

[17] A. I. König, R. Sorkin, A. Alon, D. Nachmias, K. Dhara, G. Brand, O. Yifrach, E. Arbely, Y. Roichman, and N. Elia, Live cell single molecule tracking and localization microscopy of bioorthogonally labeled plasma membrane proteins, Nanoscale **12**, 3236 (2020).

[18] V. Bayle, J.-B. Fiche, C. Burny, M. P. Platre, M. Nollmann, A. Martinière, and Y. Jaillais, Single-particle tracking photoactivated localization microscopy of membrane proteins in living plant tissues, Nat. Protoc. **16**, 1600 (2021).

[19] X. Michalet, Mean square displacement analysis of single-particle trajectories with localization error: Brownian motion in an isotropic medium, Phys. Rev. E **82**, 041914 (2010).

[20] X. Michalet and A. J. Berglund, Optimal diffusion coefficient estimation in single-particle tracking, Phys. Rev. E **85**, 061916 (2012).

[21] G. Muñoz-Gil, G. Volpe, M. A. Garcia-March, E. Aghion, A. Argun, C. B. Hong, T. Bland, S. Bo, J. A. Conejero, N. Firbas, Ò. Garibo i Orts, A. Gentili, Z. Huang, J.-H. Jeon, H. Kabbech, Y. Kim, P. Kowalek, D. Krapf, H. Loch-Olszewska, M. A. Lomholt, J.-B. Masson, P. G. Meyer, S. Park, B. Requena, I. Smal, T. Song, J. Szwabiński, S. Thapa, H. Verdier, G. Volpe, A. Widera, M. Lewenstein, R. Metzler, and C. Manzo, Objective comparison of methods to decode anomalous diffusion, Nat. Commun. **12**, 6253 (2021).

[22] S. Park, S. Thapa, Y. Kim, M. A. Lomholt, and J.-H. Jeon, Bayesian inference of Lévy walks via hidden Markov models, J. Phys. A: Math. Theor. **54**, 484001 (2021).

[23] S. Thapa, S. Park, Y. Kim, J.-H. Jeon, R. Metzler, and M. A. Lomholt, Bayesian inference of scaled versus fractional Brownian motion, J. Phys. A: Math. Theor. **55**, 194003 (2022).

[24] R. Metzler, J.-H. Jeon, A. G. Cherstvy, and E. Barkai, Anomalous diffusion models and their properties: Non-stationarity, non-ergodicity, and ageing at the centenary of single particle tracking, Phys. Chem. Chem. Phys. **16**, 24128 (2014).

[25] R. Metzler, T. Koren, B. van den Broek, G. J. L. Wuite, and M. A. Lomholt, And did he search for you, and could not find you? J. Phys. A: Math. Theor. **42**, 434005 (2009).

[26] E. Barkai, Y. Garini, and R. Metzler, Strange kinetics of single molecules in living cells, Phys. Today **65**(8), 29 (2012).

[27] Y. Liu, X. Long, P. R. Martin, S. G. Solomon, and P. Gong, Lévy walk dynamics explain gamma burst patterns in primate cerebral cortex, Commun. Biol. **4**, 739 (2021).

[28] I. Y. Wong, M. L. Gardel, D. R. Reichman, E. R. Weeks, M. T. Valentine, A. R. Bausch, and D. A. Weitz, Anomalous Diffusion Probes Microstructure Dynamics of Entangled F-Actin Networks, Phys. Rev. Lett. **92**, 178101 (2004).

[29] D. W. Sims, E. J. Southall, N. E. Humphries, G. C. Hays, C. J. A. Bradshaw, J. W. Pitchford, A. James, M. Z. Ahmed, A. S. Brierley, M. A. Hindell, D. Morritt, M. K. Musyl, D. Righton, E. L. C. Shepard, V. J. Wearmouth, R. P. Wilson, M. J. Witt, and J. D. Metcalfe, Scaling laws of marine predator search behaviour, Nature (London) **451**, 1098 (2008).

[30] I. Rhee, M. Shin, S. Hong, K. Lee, S. J. Kim, and S. Chong, On the Lévy-walk nature of human mobility, IEEE/ACM Transactions on Networking **19**, 630 (2011).

[31] G. Ariel, A. Rabani, S. Benisty, J. D. Partridge, R. M. Harshey, and A. Be'er, Swarming bacteria migrate by Lévy walk, Nat. Commun. **6**, 8396 (2015).

[32] D. W. Sims, N. E. Humphries, N. Hu, V. Medan, and J. Berni, Optimal searching behaviour generated intrinsically by the central pattern generator for locomotion, eLife **8**, e50316 (2019).

[33] R. E. Thompson, D. R. Larson, and W. W. Webb, Precise nanometer localization analysis for individual fluorescent probes, Biophys. J. **82**, 2775 (2002).

[34] N. Bobroff, Position measurement with a resolution and noise-limited instrument, Rev. Sci. Instrum. **57**, 1152 (1986).

[35] T. Savin and P. S. Doyle, Static and dynamic errors in particle tracking microrheology, Biophys. J. **88**, 623 (2005).

[36] A. J. Berglund, Statistics of camera-based single-particle tracking, Phys. Rev. E **82**, 011917 (2010).

[37] D. S. Martin, M. B. Forstner, and J. A. Käs, Apparent subdiffusion inherent to single particle tracking, Biophys. J. **83**, 2109 (2002).

[38] E. Kepten, I. Bronshtein, and Y. Garini, Improved estimation of anomalous diffusion exponents in single-particle tracking experiments, Phys. Rev. E **87**, 052713 (2013).

[39] K. Burnecki, E. Kepten, Y. Garini, G. Sikora, and A. Weron, Estimating the anomalous diffusion exponent for single particle tracking data with measurement errors—an alternative approach, Sci. Rep. **5**, 11306 (2015).

[40] I. B. Aban, M. M. Meerschaert, and A. K. Panorska, Parameter estimation for the truncated Pareto distribution, J. Am. Stat. Assoc. **101**, 270 (2006).

[41] M. L. Huang, V. Coia, and P. Brill, A cluster truncated Pareto distribution and its applications, ISRN Probability and Statistics **2013**, 265373 (2013).

[42] J. Sharpe and M. A. Juárez, Estimation of the Pareto and related distributions—a reference-intrinsic approach, Commun. Stat. Theory Methods (2021).

[43] F. P. Schoenberg and R. D. Patel, Comparison of Pareto and tapered Pareto distributions for environmental phenomena, Eur. Phys. J. Spec. Top. **205**, 159 (2012).

[44] S. Yu, A. Klaus, H. Yang, and D. Plenz, Scale-invariant neuronal avalanche dynamics and the cut-off in size distributions, PLoS ONE **9**, e99761 (2014).

[45] A. L. Efros and D. J. Nesbitt, Origin and control of blinking in quantum dots, Nat. Nanotechnol. **11**, 661 (2016).

[46] O. Flomenbom and R. J. Silbey, Utilizing the information content in two-state trajectories, Proc. Natl. Acad. Sci. USA **103**, 10907 (2006).

[47] S. A. McKinney, C. Joo, and T. Ha, Analysis of single-molecule FRET trajectories using hidden Markov modeling, Biophys. J. **91**, 1941 (2006).

[48] D. S. White, M. P. Goldschen-Ohm, R. H. Goldsmith, and B. Chanda, Top-down machine learning approach for high-throughput single-molecule analysis, eLife **9**, e53357 (2020).

[49] V. Zaburdaev, S. Denisov, and J. Klafter, Lévy walks, Rev. Mod. Phys. **87**, 483 (2015).

[50] H. Stehfest, Algorithm 368: Numerical inversion of Laplace transforms [D5], Commun. ACM **13**, 47 (1970).

[51] A. Kuznetsov, On the convergence of the Gaver-Stehfest algorithm, SIAM J. Numer. Anal. **51**, 2984 (2013).

[52] M. Magdziarz and T. Zorawik, Aging ballistic Lévy walks, Phys. Rev. E **95**, 022126 (2017).

[53] A. P. Prudnikov, Yu. A. Brychkov, and O. I. Marichev, *Integrals and Series: Elementary Functions, Vol. 1* (Gordon & Breach Science Publishers, New York, 1986).

[54] H. Y. Park, H. Lim, Y. J. Yoon, A. Follenzi, C. Nwokafor, M. Lopez-Jones, X. Meng, and R. H. Singer, Visualization of dynamics of single endogenous mRNA labeled in live mouse, Science **343**, 422 (2014).

[55] To measure the best fit, we evaluated the root-mean-squared error (RMSE) for each fit. With the ETPL [Eq. (14)] the RMSE equals 0.215 while it is 0.24 with the power law Eq. (7). With our theory [Eq. (17)] the RMSE is 0.178, smaller than the two cases, even though it is a single-parameter fit.

[56] M. de Jager, F. J. Weissing, P. M. J. Herman, B. A. Nolet, and J. van de Koppel, Lévy walks evolve through interaction between movement and environmental complexity, Science **332**, 1551 (2011).

[57] V. A. A. Jansen, A. Mashanova, and S. Petrovskii, Comment on "Lévy walks evolve through interaction between movement and environmental complexity", Science **335**, 918 (2012).

[58] A. M. Reynolds, Mussels realize Weierstrassian Lévy walks as composite correlated random walks, Sci. Rep. **4**, 4409 (2014).

[59] L. Devroye, *Non-Uniform Random Variate Generation* (Springer, New York, 1986).

[60] V. Aurich and J. Weule, Non-linear Gaussian filters performing edge preserving diffusion, in *Mustererkennung 1995*, edited by G. Sagerer, S. Posch, and F. Kummert (Springer, Berlin, 1995), pp. 538–545.